JOURNAL OF ELECTROMAGNETIC ENGINEERING AND SCIENCE, VOL. 24, NO. 2, 161~169, MAR. 2024

https://doi.org/10.26866/jees.2024.2.r.216
ISSN 2671-7263 (Online) · ISSN 2671-7255 (Print)

Near-Field Radar Equation Based on Fresnel Diffraction Formula to Detect Short-Ranged Targets for Automotive Radar

Kyoung-Sub Oh[1] · Pei-Yuan Qin[2] · Dong-Wook Seo[3,*]

Abstract

Although the classic radar equation has been widely used to analyze the link budget of an automotive radar, it is valid only when the targets are located in the far-field region of the transmitted field and the receiving antenna is located in the far-field region of the scattered field. This paper confirms this hypothesis using measured and simulated data for short-range radars. Furthermore, a novel radar equation based on the Fresnel diffraction formula is proposed for application in situations where the receiving antenna is located in the radiative near-field region (or Fresnel region) of a target, but the target is situated in the far-field region of the transmitting antenna. In addition, the proposed radar equation is assessed by comparing the measured and simulated data.

Key Words: Automotive Radar, Human Detection, Near Field, Radar Equation, Short-Range Radar.

I. INTRODUCTION

The automotive radar, generally categorized as long-range, mid-range, and short-range radars (LRR, MRR, and SRR, respectively), are an indispensable part of autonomous cars. For a decade, LRRs and SRRs have been developed to operate at 76–77 GHz [1] and 77–81 GHz [2, 3], respectively. Specifically, SRRs are usually employed to detect short-range targets, such as humans, to avoid collisions or crashes. Furthermore, as shown in Fig. 1, they typically have a quasi-monostatic structure.

The design phase of a radar system first involves conducting a link budget analysis. In this context, many researchers have continued to use the following classic radar equation for the development of an SRR [4, 5]:

$$P_r = \frac{P_t G_t}{4\pi R^2} \cdot \frac{\sigma}{4\pi R^2} \cdot A_{er} = \frac{P_t G_t G_r \sigma \lambda^2}{(4\pi)^3 R^4}, \tag{1}$$

where P_t and P_r denote the transmitted and received powers, respectively, and G_t and G_r refer to the gain of the transmitting and receiving antennas, respectively. Furthermore, σ is the radar cross section (RCS) of a target in m^2 and A_{er} indicates the effective area of the receiving antenna, which usually becomes $G_r\lambda^2/(4\pi)$. In addition, λ is the transmitted wavelength, R is the distance between the radar and the target, and $R_t \fallingdotseq R_r \equiv R$ for the quasi-monostatic radar. The most significant feature of (1) is that the received power decreases as the fourth power of R. However, this equation is valid only under conditions where the receiving antenna is situated far

Manuscript received March 09, 2023 ; Revised June 22, 2023 ; Accepted October 18, 2023. (ID No. 20230309-051J)
[1]Smart Radar System Inc., Seongnam, Korea.
[2]Global Big Data Technologies Centre, Faculty of Engineering and Information Technology, University of Technology Sydney, Ultimo, Australia.
[3]Division of Electronics and Electrical Information Engineering/Interdisciplinary Major of Maritime AI Convergence, Korea Maritime & Ocean University, Busan, Korea.
[*]Corresponding Author: Dong-Wook Seo (e-mail: dwseo@kmou.ac.kr)

from the target and the target is also located at a substantial distance from the transmitting antenna.

Similarly, in the field of wireless communication, since users or scatterers are usually located in the near-field region of the reconfigurable intelligent surface (RIS) due to its large physical dimension, research on beam focusing, localization, and channel model of the RIS has received substantial attention [6, 7].

Through its measurement and simulation results, this paper highlights that the above-mentioned conditions are not satisfied when an SRR detects humans or cars at a short distance. Furthermore, it proposes a near-field radar equation by drawing on near-field characteristics and validates it using the measured and simulation results

II. Effect of Large Target

It is well known that in circumstances where the maximum dimension D of an antenna is larger than its wavelength, the regions of the electromagnetic field around the antenna can be divided into the reactive near-field, radiative near-field (Fresnel), and far-field (Fraunhofer) regions. The most well-known boundaries between these three regions are $0.62(D^3/\lambda)^{0.5}$ and $2D^2/\lambda$ [8]. Additionally, the $D^2/4\lambda$ and $0.6D^2/\lambda$ criteria have also been frequently cited in estimating the extent of near-field and transition (Fresnel) regions [9].

In conventional numerical techniques, such as physical optics and method of moment, the first step involves obtaining the induced current on a scatterer, based on which the scattered field is calculated, from the incident field. This concept is commonly considered when calculating scattered fields from a target [10] and designing reflector antennas [11].

Fig. 1 depicts the application of this relationship between the induced current and the scattered field on a general radar target. If the electromagnetic wave generated by current J_t on the transmitting antenna results in forward propagation of the

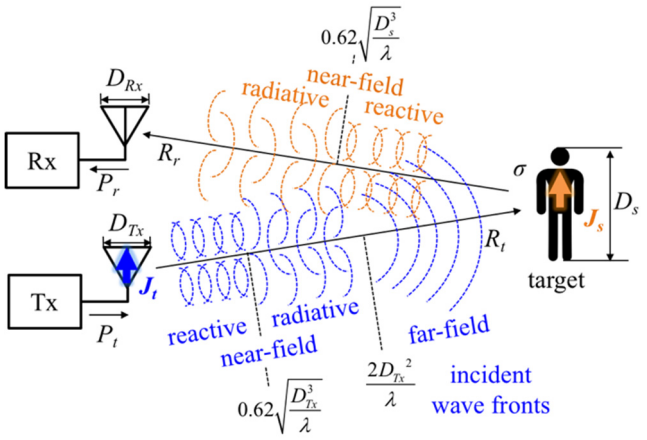

Fig. 1. Illustration of the radar and geometry for deriving the radar range equation.

target located in the far-field region, it can be considered that a uniform plane wave is incident on the target. This incident wave induces current J_s on the target, after which the induced current generates a scattered field. These sequences can also be calculated using the surface equivalence principle and radiation integrals [8]. In this context, it should be noted that the target in this example acts as an antenna with dimension D_s due to the induced current J_s. Therefore, even when the target is located in the far-field region of the transmitting antenna, the receiving antenna may not be within the far field of the target due to the target's dimensions.

Fig. 2 presents the two boundaries in the near and far scattered fields from a target with respect to the target dimension. For automotive radar tests, corner reflectors are generally used as substitutes for real targets, such as humans and other vehicles. This study used corner reflectors of dimensions 25 mm and 180 mm, characterized by RCS values of about -10 and 25 dBsm at 79 GHz, respectively, representing the values for a child and a bus. Since corner reflectors exhibit high RCS for small sizes, the far-field distance was observed to be only several meters. For the 25 dBsm reflectors, a distance of only 5–18 m was required for the far-field region. Therefore, it can be assumed that the receiving antenna is located in the far-field region. However, real targets that need to be detected by SRRs are usually much larger than corner reflectors, ranging from a 1-m-tall child to a 3.5-m-high bus.

The scattered field from a human body is predominantly determined by the upper body rather than the legs. As a result, the effective target dimensions of a 1-m-tall child and a 1.7-m-tall adult might be smaller than their actual heights. Similarly, the effective target dimensions of a 1.5-m-high car and a 3.5-m-high bus need to account for gaps between the road and the vehicle floor, rounded bodywork, and windshields. As shown in Fig. 2(b), for a receiving antenna to be located in the far-field region of a 1-m-tall child, it should be situated more than 50 m away from the child. In this context, a maximum detectable range (MDR) of 30 m for SRRs would ensure that the receiving antenna is within the reactive near-field region of the real targets. In other words, the scattered field from real targets cannot be incident on the receiving antenna in a plane wave. This means that (1) cannot estimate the exact received power in such situations, leading to an inaccurate link budget analysis for short-range targets.

This study also confirmed the effects of a large target through electromagnetic simulations using CST Microwave Studio's Integral Equation Solver. For this purpose, a simple square perfect electric conductor (PEC) plate was considered the target in the far-field region of the transmitting antenna with an operating frequency of 79 GHz. It was assumed that a plane wave is incident on the target, as shown in Fig. 3(a). By varying the tar-

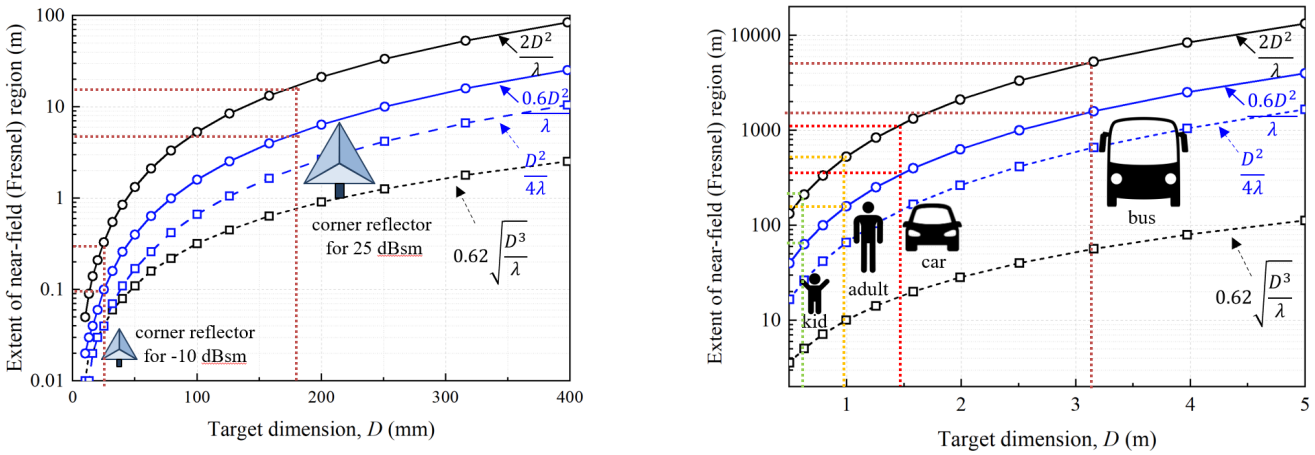

(a) (b)

Fig. 2. Minimum distance for the near- and far-field regions as a function of the dimensions of (a) corner reflectors for radar tests and (b) real targets for automotive radars.

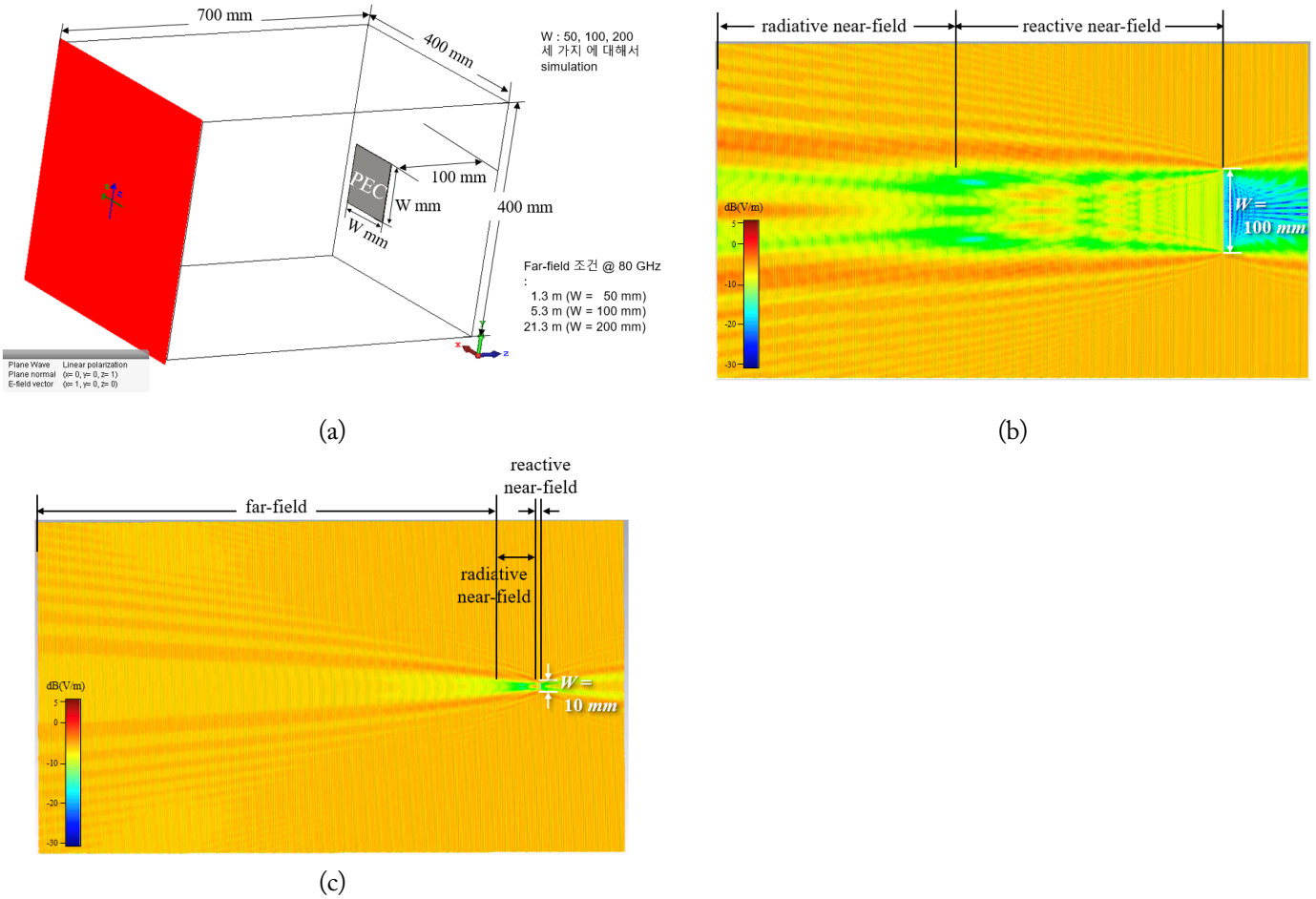

(a) (b)

(c)

Fig. 3. Geometry for simulation of the scattered field for (a) square PEC plates, and the electric field distribution for (b) PEC plate with a width of 100 mm and (c) PEC plate with a width of 10 mm.

get size W based on a fixed simulation dimension, the electric field distribution was calculated with respect to the distance from the target. Fig. 3(b) and 3(c) show the total field (i.e., both the incident and the scattered fields) covered by PEC rectangular plates with widths of 100 mm and 10 mm, respectively. In this context, it should be noted that the total field patterns of the two cases are entirely different. As expected, the electric field generated by the larger scatterer exhibits fluctuating characteristics in the reactive near-field region, as well as a characteristic decrease after a slight increase in the radiative near-field region.

This further indicates that the entire analysis region is in the near-field region. In contrast, the small scatterer exhibited a very short near-field region.

Fig. 4 presents the scattered fields obtained by removing the incident field from the total field along the central perpendicular axis of the scatterer for several rectangular scatterers. Since the analysis regions for rectangular plates of W = 50, 100, and 200 mm are in their near-field regions, their scattered fields fluctuate around 0 dB and remain fairly constant at various distances from the scatterer. Similar results have been reported in [12]. In contrast, the scattered field created by the small scatterer with W = 10 mm decreases proportionally with the inverse-square of distance ($1/R^2$) from around five wavelengths after fluctuation, which is closer to $0.6D^2/\lambda$ than $2D^2/\lambda$.

This study also verified the effects of a large target on the scattered field through conducting experiments in which a selected radar module had to detect an adult with regard to variations in radar module height, as shown in Fig. 5. Since this radar module involved an SRR and was developed to be mounted on large vehicles, such as buses and heavy vehicles, its height was modified rather than the range of the target. Furthermore, in this radar module, the receiving and transmitting antennas possessed the same structure and gain, $G_t(\theta) = G_r(\theta)$, while a constant false alarm was used to detect the target against background noise and clutter. Table 1 presents the measured MDR results obtained for several radar module heights.

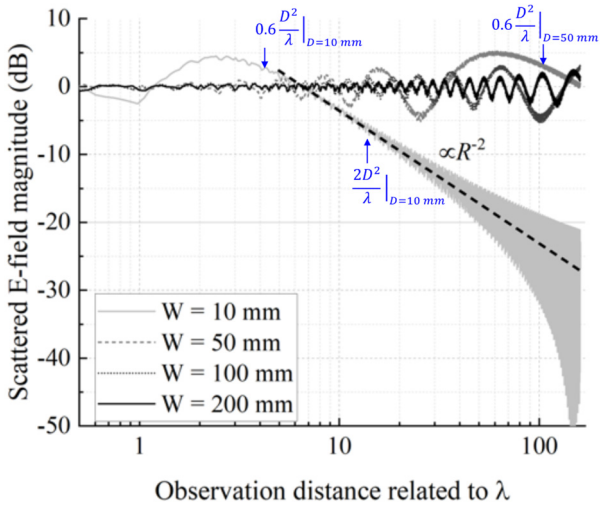

Fig. 4. Scattered field magnitude with respect to the observation distance related to one wavelength.

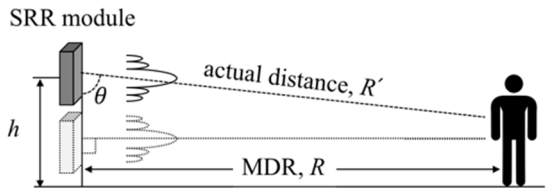

Fig. 5. Setup for measurement of the MDR of the SRR.

Since the changes in the height of the radar were smaller compared to the distance between the radar and a human target, the constant RCS and distance R' were regarded as σ and MDR R, respectively. Meanwhile, the angle of direction to the target registered a maximum 4° difference depending on the radar height. Since automotive radars generally possess a narrow beam width at an elevation angle to achieve high antenna gain, the detectable range changes in relation to the radar module height can primarily be attributed to antenna gain in the direction of the target.

In this context, the incident power density at the target can be expressed as [13, Eq. (1)]:

$$P_t \frac{G_t(\theta)}{4\pi R^2} = \frac{|E(R,\theta)|^2}{\eta}, \tag{2}$$

where E is the far-field strength in V/m and η represents the wave impedance. Furthermore, if the classic radar equation is effective in this situation, the received power scattered from the target located at the MDR can be formulated using (1) and (2), as follows:

$$\begin{aligned} P_r(R_{\max},\theta) &= \frac{P_t G_t}{4\pi R^2} \cdot \frac{G_r}{4\pi R^2} \cdot \frac{\sigma\lambda^2}{4\pi} \\ &= \frac{|E(R_{\max},\theta)|^2}{\eta} \cdot \frac{|E(R_{\max},\theta)|^2}{P_t \cdot \eta} \cdot \frac{\sigma\lambda^2}{4\pi}, \end{aligned} \tag{3}$$

which indicates the smallest received power above the detection threshold relative to the noise and clutter signal, referred to as the minimum detectable signal (MDS) [14]. The MDS of (3) generally remains unchanged unless there are significant fluctuations in the noise or clutter signal. If the classic radar equation in (3) is valid for a large target, as in the case of this experiment, the electric field strength $|E(R_{\max},\theta)|$ must be identical at all MDRs, since P_t and σ are also constant.

To obtain $|E(R_{\max},\theta)|$ at the MDRs, only the target was removed from the setup presented in the actual experiment, after which the electric field from the radar antenna was simulated using the CST Microwave Studio. Fig. 6 illustrates the simulated electric field strength at the MDRs listed in Table 1. At the center frequency of 79 GHz, the electric field strength presents different values for the MDRs. This indicates that the classic radar equation is unsuitable for a large target. Therefore, a new radar equation is required for situations in which the receiving antenna is located in the near-field region of the target.

III. Near-Field Radar Equation

1. Formulation

To formulate a new radar equation for the near-field region, propagation characteristics in the region had to be formulated. To

Table 1. Measured MDR for a 1.72-m-tall adult with respect to several radar module heights

	Radar height, h (m)				
	1.1	1.5	1.7	2.0	2.2
MDR, R_{max} (m)	23	21	19.4	19.0	17
Actual distance, R' (m)	23.00	21.01	19.42	19.03	17.05
Angle, θ (°)	89.4	88.3	87.6	86.6	85.5

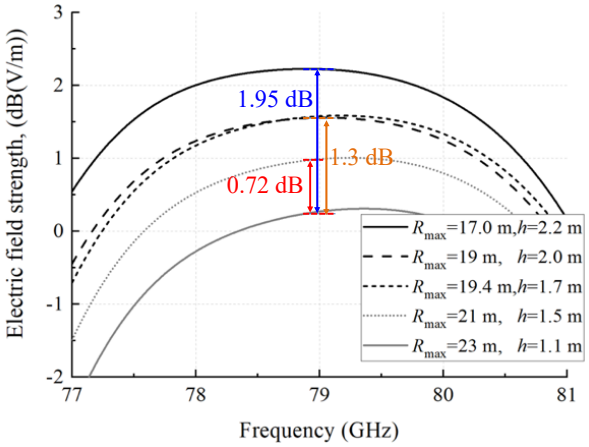

Fig. 6. Electric field strength (20log|E|) at the MDRs.

simplify this problem, a rectangular plate was considered the target, as shown in Fig. 7(a). According to Love's equivalence principle, an aperture of width T_w and height T_h in an infinite ground plane and a plate of width T_w and height T_h in free space are complementary structures, as shown in Fig. 7(b). Therefore, the scattered field can be obtained from field E_0 on the aperture instead of the current density J_s on the metal plate.

Based on the assumption that the observation point is located farther from the target's dimensions, $(x-x')^2+(z-z')^2 \ll y^2$. Therefore, the distance from the origin of the aperture can be approximated as follows:

$$r = [y^2+(x-x')^2+(z-z')^2]^{\frac{1}{2}} \approx y + \frac{(x-x')^2+(z-z')^2}{2y}, \quad (4)$$

Based on the assumption in (4), the field strength in the near-field region can be obtained from the Fresnel diffraction formula [15] as follows:

$$E(x,y,z) = \frac{jk}{2\pi y} e^{-jky} \cdot \int_{-\frac{T_h}{2}}^{\frac{T_h}{2}} \int_{-\frac{T_w}{2}}^{\frac{T_w}{2}} E_0(x',z') e^{-jk\frac{(x-x')^2+(z-z')^2}{2y}} dx'dz', \quad (5)$$

where field $E_0(x',z')$ in the aperture represents a part of the incident field from the transmitter. Therefore, from (2), $E_0(x',z')$ can be expressed as:

$$E_0(x',z') = \sqrt{\eta P_t \frac{G_t(R,\theta)}{4\pi R^2}} \times \Gamma, \quad (6)$$

where Γ is the reflection coefficient of the target, which is dependent on the incident and scattered angles, as well as the material characteristics of the target.

Furthermore, if field $E_0(x',z')$ is uniformly distributed in the aperture, it becomes a constant value of E_0. In such a case, the scattered field can be formulated as follows:

$$E(x,y,z) = j\frac{E_0}{2} e^{-jky} \sqrt{\frac{k}{\pi y}} \int_{-\frac{T_w}{2}}^{\frac{T_w}{2}} e^{-jk\frac{(x-x')^2}{2y}} dx' \cdot \sqrt{\frac{k}{\pi y}} \int_{-\frac{T_h}{2}}^{\frac{T_h}{2}} e^{-jk\frac{(z-z')^2}{2y}} dz', \quad (7)$$

Subsequently, using the complex Fresnel integral F(z), the field can be attained from the following equation:

$$E(x,y,z) = j2E_0 e^{-jky} F\left(\frac{T_w}{2}q\right) F\left(\frac{T_h}{2}q\right), \quad (8)$$

where the complex Fresnel integral $F(z)$ and parameter q can be defined as:

$$F(z) = \int_0^z e^{-j\frac{\pi}{2}t^2} dt, \quad (9)$$

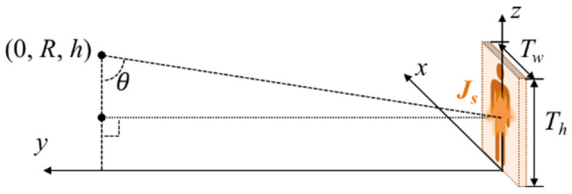

(a)

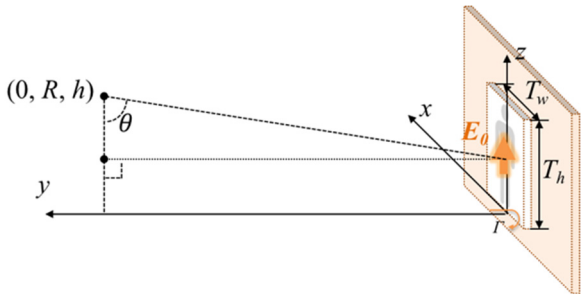

(b)

Fig. 7. Geometry for Fresnel diffraction from (a) a thin plate, and (b) a thin aperture in an infinite conducting plane.

$$q = \sqrt{\frac{k}{\pi y}} = \sqrt{\frac{2}{\lambda y}}. \tag{10}$$

Notably, the Fresnel integral in (9) can be calculated using the approximation equations noted in Appendix A.

Effectively, the electric field at the height of the radar at distance R away from the aperture can be presented as follows:

$$E(0,R,z) = j2E_0 e^{-jkR} F\left(\frac{T_w}{2}q\right) F\left(\frac{T_h}{2}q\right). \tag{11}$$

In addition, by multiplying the scattered power and the receiving antenna aperture area, the received power can be estimated as follows:

$$P_r = \frac{|E(0,R,z)|^2}{\eta} A_{er} = \frac{|E(0,R,z)|^2}{\eta} \cdot \frac{\lambda^2 G_r(\theta)}{4\pi}. \tag{12}$$

Again, substituting (6) and (11) into (12) yields the following equation:

$$P_r = P_t \frac{G_t(\theta) G_r(\theta) \lambda^2}{(4\pi R)^2} |\Gamma|^2 \left|2F\left(\frac{T_w}{2}q_R\right) F\left(\frac{T_h}{2}q_R\right)\right|^2 \tag{13}$$

where $q_R = (2/\lambda R)^{0.5}$. In this context, it should be noted that the derived near-field radar equation in (13) would be valid only when the distance between the observation point and the target is greater than the target dimension, i.e., in the Fresnel region, due to (4).

Furthermore, by comparing (13) and (1), the near-field RCS of the target can be expressed as:

$$\sigma_{\text{near-field}} = |\Gamma|^2 \left|2F\left(\frac{T_w}{2}q_R\right) F\left(\frac{T_h}{2}q_R\right)\right|^2. \tag{14}$$

Fig. 8 depicts the received power, calculated using (13), with respect to the distance between the radar and the target. This calculation assumed that the receiving module is placed at distance R from the plate at a height of 1.72 m, bearing a width of 0.55 m. As depicted in Fig. 8, the received power declines up to approximately 70 m, after which the square of distance begins to decrease stably until the fourth of the distance reaches about 400 m, which is closer to $0.6D^2/\lambda$ than $2D^2/\lambda$. Notably, the results obtained for the near-field region contrast sharply with those of the classic radar equation in the far-field region. In addition, the near-field radar equation in (14) can be applied to both far-field and near-field regions. Notably, if the receiving antenna is located in the far-field region of the target, the equation in (14) will become the classic radar equation presented in (1). This transformation process is detailed in Appendix B.

2. Verification with Simulated and Experimental Data

As mentioned earlier, considering the same false alarm rate and transmitted power, the received power at the MDR should be as constant as the MDS. Therefore, to verify the proposed near-field radar equation in (13), the received power at some MDRs was calculated to confirm whether they had identical received power.

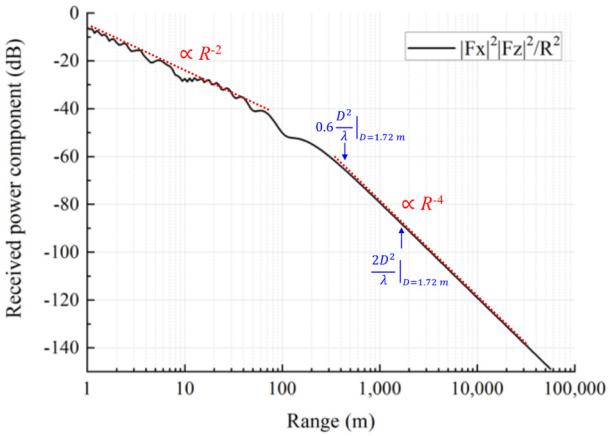

Fig. 8. Received power component as a function of the distance between the receiving antenna and the plate target.

The received power was calculated by incorporating the measurement results in Table 1 and the simulated results in Fig. 6 into the near-field radar equation in (13). However, since the transmitted power and reflection coefficient data of a human were not available, the received power ratio was calculated rather than the absolute received power. Notably, if the proposed near-field radar equation is valid, the received power ratio would be either 1.0 or 0 dB. In this context, the ratio of the received power in $R_{\max 1}$ and $R_{\max 2}$ can be expressed as follow:

$$\frac{P_r(R_{\max 1},\theta)}{P_r(R_{\max 2},\theta)} \approx \frac{|E(R_{\max 1},\theta)|^2}{|E(R_{\max 2},\theta)|^2} \cdot \frac{\left|F\left(\frac{T_w}{2}q_{R_{\max 1}}\right) F\left(\frac{T_h}{2}q_{R_{\max 1}}\right)\right|^2}{\left|F\left(\frac{T_w}{2}q_{R_{\max 2}}\right) F\left(\frac{T_h}{2}q_{R_{\max 2}}\right)\right|^2} \tag{15}$$

where the first term on the right side of the equation—the electric field strength—is obtained from the simulated results presented in Fig. 6, while the second term is calculated using the approximation solution in (A1)–(A7) for each radar height and MDR. These results are summarized in Table 2, where the RCS component and received power component are expressed as $|E(R_{\max},\theta)|^2$ and $|E(R_{\max 1},\theta)|^2 \cdot \left|F\left(q_{R_{max}} T_w/2\right)\right|^2$ the right side of the equation in (15), respectively.

The fifth row in Table 2 notes the ratio of the received power at the radar height to that at 1.5-m height in the near-field, calculated using (15). Since the power level fluctuates instead of decreasing smoothly as the distance increases in the near-field region, and because the variability caused by the inaccurate target height is large, the received powers are not observed to be identical to each other. However, they showed similar values, with an error of less than 0.3 dB. This indicates that the proposed near-field radar equation is in good agreement with the measured MDRs for several SRR module heights.

Table 2. Received power component values at measured MDR for several radar module heights

	Radar height, h (m)				
	1.1	1.5	1.7	2.0	2.2
E-field at target (dB)	0.27	0.99	1.58	1.56	2.22
Near field region					
RCS component (dB)	3.01	2.19	1.34	1.81	1.13
Received power component (dB)	3.28	3.18	2.92	3.37	3.35
$P_r(R,\theta)/P_r(1.5\text{m},\theta)$	0.10	-	0.26	0.19	0.17
Far field region					
RCS component (dB)	23.20	22.35	22.17	21.48	20.69
Received power component (dB)	25.42	23.91	23.75	22.47	20.96
$P_r(R,\theta)/P_r(1.5\text{m},\theta)$	1.51	-	0.16	1.44	2.95

Furthermore, assuming that the receiving antenna is located far from the target, the far-field RCS of the target was obtained from (B7). The far-field values corresponding to the RCS and the received power components in the near field are listed in rows 6–8 of Table 2. The results show that although the received power and the MDR should be almost the same, a maximum error of about 3 dB is observed. In addition, the fourth power relation between the received power and the target range is the result of having an excessively larger received power component value than the actual value in the near field. This highlights that existing far-field radar equations pertaining to the near field are inaccurate.

IV. Conclusion

This study proposed a novel near-field radar equation that is valid in the Fresnel region based on the Fresnel diffraction formula. The major feature of this equation is that the dependency of the distance between the radar and its targets is not considered as the negative fourth power of the distance, but as its negative square. Notably, various MDRs could be explained by the application of the proposed radar equation to the measurement results. However, to achieve a more accurate analysis of automotive radars, such as SRRs, further research on near-field receiving antenna gain and RCS is necessary.

This research was supported by the Basic Science Research Program through the National Research Foundation of Korea (NRF), funded by the Ministry of Education (No. 2021R1I1A3044405).

Appendix

A. Approximation Solution of Complex Fresnel Integral

The complex Fresnel integral $F(z)$ can be expressed as the combination of two Fresnel integrals, $C(z)$ and $S(z)$, as follows:

$$F(z)=\int_0^z e^{-j\frac{\pi}{2}t^2}dt=C(z)-jS(z), \tag{A1}$$

where $C(z)$ and $S(z)$ are the Fresnel integrals, which can be defined as follows:

$$C(z)=\int_0^z \cos\left(\frac{\pi}{2}t^2\right)dt, \tag{A2}$$

$$S(z)=\int_0^z \sin\left(\frac{\pi}{2}t^2\right)dt. \tag{A3}$$

These two Fresnel integrals can be solved using various methods, such as series expansion, asymptotic expansion, relation to error, hypergeometric function, and spherical Bessel function. Furthermore, Fresnel integrals can be calculated using approximation equations [16].

Fresnel integrals can also be expressed using auxiliary functions, such as:

$$C(z)=\frac{1}{2}+f(z)\sin\left(\frac{\pi}{2}z^2\right)-g(z)\cos\left(\frac{\pi}{2}z^2\right), \tag{A4}$$

$$S(z)=\frac{1}{2}\pm f(z)\cos\left(\frac{\pi}{2}z^2\right)-g(z)\sin\left(\frac{\pi}{2}z^2\right), \tag{A5}$$

where auxiliary functions $f(x)$ and $g(x)$ can be approximately expressed as:

$$f(x)=\frac{1+0.926x}{2+1.792x+3.104x^2}+\varepsilon(x), \tag{A6}$$

$$g(x)=\frac{1}{2+4.142x+3.492x^2+6.670x^3}+\varepsilon(x), \tag{A7}$$

in which $|\varepsilon(x)|\le 2\times10^{-3}$ for $0\le x\le\infty$.

B. Transformation of the Near-Field Radar Equation into the Classic Radar Equation for Long Distances

The assumption that the receiving antenna is located in the far-field region of the target can be represented as:

$$R>\max\left\{\frac{2T_w^2}{\lambda},\frac{2T_h^2}{\lambda}\right\}. \tag{B1}$$

Considering this, the variables of the Fresnel integrals can be denoted as:

$$\frac{T_w}{2}q_R=\frac{T_w}{2}\sqrt{\frac{2}{\lambda R}}=\sqrt{\frac{T_w^2}{2\lambda R}}, \tag{B2}$$

$$\frac{T_h}{2}q_R=\frac{T_h}{2}\sqrt{\frac{2}{\lambda R}}=\sqrt{\frac{T_h^2}{2\lambda R}}. \tag{B3}$$

When substituting (B1) into (B2) and (B3), the variables of

the Fresnel integral should be less than 0.5. Therefore, the Fresnel integral can be approximated as follows:

$$F\left[\frac{T_w}{2}q_R\right] = \int_0^{\sqrt{\frac{T_w^2}{2\lambda R}}} e^{-j\frac{\pi}{2}t^2}dt$$
$$\cong \int_0^{\sqrt{\frac{T_w^2}{2\lambda R}}} \left(1 - j\frac{\pi}{2}t^2\right)dt = \sqrt{\frac{T_w^2}{2\lambda R}}\left(1 - j\frac{\pi}{6}\frac{T_w^2}{2\lambda R}\right). \quad \text{(B4)}$$

Similarly, another Fresnel integral term in (12) becomes the following:

$$F\left[\frac{T_h}{2}q_R\right] \cong \sqrt{\frac{T_h^2}{2\lambda R}}\left(1 - j\frac{\pi}{6}\frac{T_h^2}{2\lambda R}\right). \quad \text{(B5)}$$

Meanwhile, substituting (B4) and (B5) into (12) gives the following equation:

$$P_r \cong P_t \frac{G_t G_r \lambda^2}{(4\pi)^3 R^4}|\Gamma|^2 \frac{4\pi T_w^2 T_h^2}{\lambda^2}. \quad \text{(B6)}$$

Thus, the near-field radar equation no longer exhibits $1/R^2$ dependency; rather, it now shows $1/R^4$ dependency. A comparison of (B6) and (1) provides the values for the near-field RCS for the metal plate:

$$\sigma = \frac{4\pi T_w^2 T_h^2}{\lambda^2}|\Gamma|^2, \quad \text{(B7)}$$

which indicates the far-field RCS of a rectangle plate with width T_w and height T_h. In addition, Eq. (B6) becomes the exact same as (1) when the RCS symbol is used.

REFERENCES

[1] Y. S. Won, D. Shin, S. Jung, J. H. Lee, C. Lee, M. Park, Y. Song K. Moon, and D. W. Seo, "Method to improve degraded range resolution due to non-ideal factors in FMCW radar," *IEICE Electronics Express*, vol. 16, no. 1, article no. 20180924, 2019. https://doi.org/10.1587/elex.15.20180924

[2] J. I. Lee, J. H. Lee, S. H. Lee, and D. W. Seo, "Low sidelobe design of microstrip comb-line array antenna using deformed radiating elements in the millimeter-wave band," *IEEE Transactions on Antennas and Propagation*, vol. 70, no. 10, pp. 9930-9935, 2022. https://doi.org/10.1109/TAP.2022.3184555

[3] J. H. Lee, S. H. Lee, H. J. Lee, J. H. Oh, J. Y. Kim, I. K. Cho, and D. W. Seo, "Design of comb-line array antenna for low sidelobe level in millimeter-wave band," *IEEE Access*, vol. 10, pp. 47195-47202, 2022. https://doi.org/10.1109/ACCESS.2022.3169280

[4] V. Jain, F. Tzeng, L. Zhou, and P. Heydari, "A single-chip dual-band 22–29-GHz/77–81-GHz BiCMOS transceiver for automotive radars," *IEEE Journal of Solid-State Circuits*, vol. 44, no. 12, pp. 3469-3485, 2009. https://doi.org/10.1109/JSSC.2009.2032583

[5] International Telecommunication Union, "Systems characteristics and compatibility of automotive radars operating in the frequency band 77.5 78 GHz for sharing studies (ITU-R M.2322-0)," 2014 [Online]. Available: https://www.itu.int/dms_pub/itu-r/opb/rep/R-REP-M.2322-2014-PDF-E.pdf.

[6] X. Li, H. Lu, Y. Zeng, S. Jin, and R. Zhang, "Near-field modeling and performance analysis of modular extremely large-scale array communications," *IEEE Communications Letters*, vol. 26, no. 7, pp. 1529-1533, 2022. https://doi.org/10.1109/LCOMM.2022.3172437

[7] H. Lu and Y. Zeng, "Communicating with extremely large-scale array/surface: unified modeling and performance analysis," *IEEE Transactions on Wireless Communications*, vol. 21, no. 6, pp. 4039-4053, 2022. https://doi.org/10.1109/TWC.2021.3126384

[8] C. A. Balanis, *Antenna Theory: Analysis and Design*, 3rd ed. Hoboken, NJ: John Wiley & Sons, 2005.

[9] Federal Communications Commission Office of Engineering & Technology, "Evaluating compliance with FCC guidelines for human exposure to radiofrequency electromagnetic fields," 1997 [Online]. Available: https://transition.fcc.gov/oet/info/documents/bulletins/oet65/oet65a.pdf.

[10] D. Y. Lee, J. I. Lee, and D. W. Seo, "Dynamic RCS estimation according to drone movement using the MoM and far-field approximation," *Journal of Electromagnetic Engineering and Science*, vol. 21, no. 4, pp. 322-328, 2021. https://doi.org/10.26866/jees.2021.4.r.40

[11] S. R. Zang and J. R. Bergmann, "Analysis of omnidirectional dual-reflector antenna and feeding horn using method of moments," *IEEE Transactions on Antennas and Propagation*, vol. 62, no. 3, pp. 1534-1538, 2014. https://doi.org/10.1109/TAP.2013.2296775

[12] S. Laybros, P. F. Combes, and H. J. Mametsa, "The "very-near-field" region of equiphase radiating apertures," *IEEE Antennas and Propagation Magazine*, vol. 47, no. 4, pp. 50-66, 2005. https://doi.org/10.1109/MAP.2005.1589874

[13] M. Kanda and R. Orr, "Near-field gain of a horn and an open-ended waveguide: comparison between theory and experiment," *IEEE Transactions on Antennas and Propagation*, vol. 35, no. 1, pp. 33-40, 1987. https://doi.org/10.1109/TAP.1987.1143963

[14] B. R. Mahafza, *Radar Systems Analysis and Design using MATLAB*, 3rd ed. Boca Raton, FL: CRC Press, 2013.

[15] A. Ishimaru, *Electromagnetic Wave Propagation, Radiation, and Scattering: From Fundamentals to Applications*, 2nd ed. Hoboken, NJ: John Wiley & Sons, 2017.

[16] M. Abramowitz and I. A. Stegun, *Handbook of Mathematical Functions with Formulas, Graphs, and Mathematical Tables*. New York, NY: Dover Publications, 1965.

Kyoung-Sub Oh
https://orcid.org/0009-0009-9002-5095

received is B.S. degree in electrical engineering from Chonbuk National University, Jeonju, South Korea, in 1994, and his M.S. and Ph.D. degrees in electrical engineering from the Korea Advanced Institute of Science and Technology (KAIST), Daejeon, South Korea, in 1997 and 2004, respectively. From 2004 to 2005, he worked for Hyundai Motor, Hwaseong, South Korea, after which he was employed in Maltani Lighting, Seoul, South Korea, from 2005 to 2008. From 2008 to 2010, he worked at Samung Electronics, Hwaseong, South Korea. He joined KAIST, Daejeon, South Korea, in 2010, where he worked until 2014, after which he was engaged at Gamma Nu, Hwasung, South Korea, until 2017. Since 2017, he has been a principal research engineer at Smart Radar System Inc., Seongnam, South Korea. His research interests include radar systems, antennas, microwave imaging, inverse scattering, and wireless communication systems.

Pei-Yuan Qin
https://orcid.org/0000-0001-8861-4143

was born in Liaoning, China, in 1983. He received his bachelor's degree in electronic engineering from Xidian University, Xi'an, China, in 2006, and a joint Ph.D. degree in electromagnetic fields and microwave technology from Xidian University and Macquarie University, Sydney, NSW, Australia, in 2012. He is currently an associate professor at the University of Technology Sydney, Ultimo, Australia. His research interests include reconfigurable antennas, antenna arrays, and microwave components.

Dong-Wook Seo
https://orcid.org/0000-0001-9449-7772

received his B.S. degree in electrical engineering from Kyungpook National University, Daegu, South Korea, in 2003, and his M.S. and Ph.D. degrees in electrical engineering from Korea Advanced Institute of Science and Technology (KAIST), Daejeon, South Korea, in 2005 and 2011, respectively. He was a senior researcher at the Defense Agency for Technology and Quality (DTaQ), Daegu, from 2011 to 2012. From 2012 to 2017, he was a senior researcher at the Electronics and Telecommunications Research Institute (ETRI), Daegu. Since September 2017, he has been a faculty member in the Division of Electronics and Electrical Information Engineering, Korea Maritime & Ocean University (KMOU), Busan, South Korea, where he is currently a professor. His research interests include numerical techniques in the areas of electromagnetics, radar cross-section analysis, wireless power transfer, and radar systems.